Late glacial to deglacial sedimentary and geochemical record from the southern chilean margin and timing of the Patagonian icefield fluctuations

Mélanie Carel*[a], Giuseppe Siani [a], Christophe Colin [a], Quentin Dubois-Dauphin [a], Stéphanie Duschamp-Alphonse [a], Catherine Kissel [b], Elisabeth Michel [b]

[a] *Université Paris Sud, Laboratoire des Interactions et Dynamique des Environnements de Surface (IDES), UMR-CNRS 8148, Bâtiment 504, 91405 Orsay Cedex, France*

[b] *Laboratoire des Sciences du Climat et de l'Environnement (LSCE), Laboratoire mixte CNRS-CEA, Avenue de la Terrasse, 91198 Gif-sur-Yvette Cedex, France.*

* Corresponding author: E-mail address: melanie.carel@u-psud.fr; Phone: +33.01.69.15.67.47

1. Introduction

One of the peculiar interests of paleoclimatic reconstructions in the high southern latitudes involves the understanding of ice dynamic and ice-sheet behaviour mostly sensitive to temperatures and precipitations variations (Denton and Karlen, 1973; Aniya and Enomoto, 1986). By the way, features of glacial terminations emphasize abrupt changes between glacial and deglacial conditions and provide invaluable informations about the forcing mechanisms of climate changes (Heusser, 1993; Wenzens, 2001). Southern Patagonia exhibits an ideal position to evidence the linkages between mid and high southern latitudes due to its windward location and the position of the two main Patagonian icecaps. Over the last decades a large wealth of studies were focused on the influence of the middle to high latitude climatic regimes and their eventual link with ice cap dynamic (Douglass et al., 2006; Kaplan et al., 2008; Moreno et al., 2009). It has also been proposed that the oulet glaciers represent substantial ice masses continuously fed by heavy rainfall driven by the southern westerlies (SWW) causing high snow accumulation and ice velocities (Roth et al., 1998).

Since the last glacial period, Patagonian icecaps have shown evidences of steady fluctuations pace, alternating between advances and retreats phases, based on geomorphological and sedimentological studies and chronological dates on terminal moraines from Southern Patagonian icecap (Aniya and Sato, 1995; Glasser et al., 2004; Kaplan et al., 2005, 2008; Douglass et al., 2005, 2006; Glasser et al., 2008) coupled to modelling of Patagonian extension during the last glacial (Wyrwoll et al., 2000; Hulton et al., 2002). Despite growing consideration on the links between glacier fluctuations and westerly winds, the mechanisms governing these events and their timing remain poorly constrained as well the origin still remains debated.

In this study, we present a new sedimentological approach based on a highly resolution terrigenous record by coupling clay mineralogy, grain-size, bulk chemistry, magnetic properties and morphological characteristics of particles from two high sedimentation rate deep-sea cores collected offshore the southern Patagonian area (46°S). The overall aim of this work is to restore southeastern Chilean margin climate variability since the last glacial maximum (LGM) encompassing northern Patagonian icecap fluctuations and their eventual link with regional and global climate. This study benefits of precise AMS ^{14}C and $\delta^{18}O$ chronology performed on the planktic foraminifera *Globigerina bulloides*. The terrigenous record based on extremely high sedimentation rates favours the reconstruction of a detailed dataset that partly solve northern icecap recession/advance timing that varies somewhat between areas, and the impact of climate variability during the last glacial/interglacial transition in the Patagonian region.

2. Geological and climatic setting

The inland physiography of the study area is characterized by two main geological units from west to east: the Coastal Range and the Andean Cordillera. The Coastal Range is constituted by

primarily potassium-rich igneous rocks and low-grade metamorphic basement whereas titanium-rich volcanics build the high reliefs of the Andean Cordillera resulting from the recent activity of the Cenozoic Andean volcanoes overlapping the Patagonian Batholith formed by Mesozoic intermediate plutonic rocks (Stern, 1984; Zeil, 1986). Resulting from the subduction of the Nazca and Antarctic plates beneath the South American plate (Minster et al., 1974; Cande et Leslie, 1986), the strong elevation of the Andes reliefs influence the pattern of the Westerlies-driven rainfall distribution, which are more intense on the western side of the Andes, reaching mean maxima of 3000-4000 mm/yr over the Andes (Miller, 1976; Fujiyoshi et al., 1987; Garreaud et Aceituno, 2007).

Offshore, the oceanography is mainly controlled by the cool Antarctic Circumpolar Current (ACC) surface component which converges towards the Chilean coast between 40 and 45°S before splitting up into two branches: the poleward Cap Horn Current (CHC) and the equatorward Humboldt Current (HC; Strub et al., 1998; Fig; 1). Deeper circulation is dominated by the flowing of the Antarctic Intermediate Waters (AAIW) between 400 and 1,200 m depth and the Pacific deep water (PDW) below (Brandhorst et al., 1971).

South Patagonian margin is climatically active because of its strategic position that intercepts the entire southern Westerly winds cell (SWW) which exerts a exclusive control on the entrance of storm tracks in the Chilean continent (Trenberth, 1991). Directly dependent of the latitudinal migration of the polar front position, the SWW was submitted to intensity changes and seasonal fluctuations varying from 40 to 60°S resulting in the modification of the distribution of the rainfall, the icefields dynamic and the oceanography.

3. Material and Methods

Calypso deep-sea cores MD07-3088 and MD07-3119 were collected during the IMAGES PACHIDERME (MD159) cruise on February 2007 by the French R/V Marion Dufresne in the South Pacific Ocean (Kissel, 2007). The first was recovered off the Taitao peninsula (46°04’30S; 75°41’23W; 1,536 m bsl; 18.9 m length) whereas the latter was collected offshore (MD07-3119, 46°05’S, 76°06’W, 3250 m bsl, 32.5 m) (Fig.1).

In this study the last 12.9 meters of the MD07-3088 core and the first 7.5 meters for MD07-3119 core are presented. The lithology of the core MD07-3088 displays predominant greyish olive to grey silty clay deposits with frequent intercalations of silty/sandy layers (Siani et al., 2010). The lithology of the core MD07-3119 is composed of homogenous clayey greyish-olive diatoms-rich layers with some intercalations of silty-sandy layers (Kissel, 2007).

3.1. Grain-size measurements

Grain-size analyses were realized on the carbonate-free sediment fraction using a laser diffraction particles analyzer Malvern Mastersizer 2000 at IDES laboratory (Université Paris Sud).

Carbonates were removed using 10% HCl solution (Trentesaux et al., 2001) and remaining residual was incorporated in the deionized water tank under 550 rpm for stirrer and 2000 rpm pump conditions. The 12.9 m of the core MD07-3088 were sampled every 2 cm representing 520 samples whereas the core MD07-3119 was sampled every 5 cm representing 109 samples.

Each sample was introduced under a beam laser obscuration close to 10%. Mastersizer 2000 mathematical software allowed to obtain distribution parameters and frequencies in respect with Folk and Ward parametric definition (1957) and measurements are expressed between 0.05 and 2,000 mm grain size classes.

For the MD07-3088 record, sampling was refined in two coarser layers (i.e. 1368 and 1558 cm) sampled every 0.5 cm at 5 cm on both sides, representing about 24 samples analyzed with a higher beam obscuration of about 15%.

3.2. Clay assemblages

Clay mineralogy was acquired by standard X-Ray diffraction (XRD) with a sampling step of 2 cm along the core MD07-3088 that represents 650 samples integrating 130 clay analyses previously determined by Siani *et al.* (2010) whereas clay minerals were identified every 5cm along the core MD07-3119.

Clay signal was performed by X-Ray PANalytical X'Pert Pro MPD diffractometer at IDES laboratory (Université Paris Sud) emitting CuKa dichromatic beam. X-Ray apparatus was adjusted to a goniometer angle of 3 to 30° 2θ range, associated to a beam conditions of 45 KeV and 40 mA and a measuring time of ~ 1 second/step. To remove carbonated fraction, samples were leached in 0.1 N hydrochloric acid solution before to be rinsed several times. Clay mineralogy was performed on the carbonate-free clayey fraction (< 2 μm) extracted from the bulk sediment according to the Stoke's law before to be mounted on oriented glass slides. Each sample was submitted to three treatments: air drying, ethylene-glycol solvation during 24 hours for each sample and heated at 510°C during 2 hours for few samples. Results are interpreted from semi-quantitative estimations of basal reflections with mean accuracy of approximately 4% and determined from abundance peaks of clay types on glycolated samples using MacDiff software (Petschick et al., 1996). Relative proportions expressed in percentages of the total clay assemblages of smectite and illite are estimated from the areas of the 17Å and 10Å peaks respectively whereas relative proportions of kaolinite and chlorite are calculated from the ratios of areas of the peaks centred at 3.57Å and 3.54Å respectively.

3.3. XRF-scanning

Inorganic geochemistry of each carbonate-free sample of the core MD07-3088 were estimated by WDS X-Ray Fluorescence Avaatech core-scanning (XRF) at the Royal Netherland Institute for Sea Research (NIOZ; Richter et al., 2006) and previously presented in Siani *et al.*, 2010. Samples were

collected every 1 cm, but in order to facilitate correlations with clay mineralogy data, only results every 2 cm were selected, representing 641 samples. In this study, the most representative elements are presented used as source proxies as K, Ti and Zr elementary contents.

3.4. Magnetic grain-size measurements

Paleomagnetic grain-size was performed continuously on the u-channel of the core MD07-3088 with a sample step of 2 cm. The magnetic parameters (susceptibility, anhysteretic remanent magnetization (ARM) and isothermal remanent magnetization (IRM) have been obtained according to the methods of Weeks et al. (1993; 1995) at the Laboratoire des Sciences du Climat et de l'Environnement (LSCE, Gif sur Yvette, France). Magnetic parameters have been acquired when sedimentary column (u-channel) was submitted to a magnetic field. ARM parameter is performed as a function of the distance of the u-channel from the demagnetizing coils. IRM parameter is acquired when the u-channel passes through the poles of an electromagnet (Weeks et al., 1993). Magnetic susceptibility translates the contribution of ferromagnetic minerals like magnetite and hematite and paramagnetic minerals like olivine, pyroxene and amphibole although ferromagnetic minerals are present in minor proportions compared to the latter (Sandgren and Snowball, 2010).

3.5. Morphoscopic analysis

To obtain clues concerning particles morphology in core MD07-3088, SEM pictures have been taken from individual handpicked particles in silty/sandy layers in the fraction > 40 μm and refined in the fraction > 150 μm. Support was constituted mainly by detrital particles such as quartz and feldspars. High-resolution imaging was realized on a Philips XL30 SEM at Université Paris Sud. Backscattered electrons beam was defined at 10 μm with accelerating voltage of 15 KeV and beam intensity of 80 mA.

4. Oxygen isotopes and radiocarbon dating

The oxygen isotopes stratigraphies of the cores MD07-3088 and MD07-3119 were established from *Globigerina bulloides* foraminifera shells in the size fraction between 250 and 315 μm with a sampling step every 5 cm to 10 cm along the core MD07-3088 and MD07-3119 respectively. Analyses were performed at LSCE on a MAT Finnigan 251 Delta+ mass spectrometer with a mean external reproductibility of 0.05 ‰ (1σ) (Duplessy, 1978). Results were then normalized according to the Vienna Pee Dee Belemnite (VPDB; Coplen, 1988).

4.1. Age model of the core MD07-3088

The age model of core MD07-3088 is based on nineteen AMS ^{14}C dates, applied on monospecific *G. bulloides* foraminifera shells (Table 1, Siani et al., 2010, 2012), in the size fraction > 150 μm. The conventional radiocarbon ages were corrected to a reservoir age correction of approximately 1,300 years for the last deglaciation and 900 years for the late glacial period, the Antarctic cold reversal (ACR) event and the Early Holocene respectively (Siani et al., 2012). The corrected radiocarbon ages were then converted into calendar ages using Oxcal 3.10 calibration software (Bronk-Ramsey et al., 2009) based on INTCAL 09 software (Reimer et al., 2009). The inferred age model allows to determine sedimentation rates reaching about 300 cm/ka during the last glacial and about 60 cm/ka during LGIT and Holocene. In parallel, tephrochronologic study reveals the presence of at least eleven tephras layers during this time interval along the marine core (Carel et al., 2011) out of which three were attributed to Hudson volcano activity (Naranjo and Stern, 1998; Haberle and Lumley, 1998) providing further chronological constraints. Hereafter, all the ages will be presented as calibrated age ka BP.

4.2. Age model of the core MD07-3119

Due to the absence of radiocarbon dates for the core MD07-3119, the age model was build by comparing the $\delta^{18}O$ record with that of the core MD07-3088 well constraints in time. Similarity in the distribution of the $\delta^{18}O$ signals between the two records allows to obtain new chronological markers for the core MD07-3119 (Fig. 2, Table 2). The oxygen isotopic record shows the last glacial interglacial transition and the Holocene encompassing the 32 meters of the core. In this study, the first 7.5 meters of the core have been analyzed covering a time interval between 18.5 to 7 ka BP. The inferred sedimentation rates were estimated at approximately 320 cm/ka during the last glacial and 50 cm/ka during LGIT similar to those obtained in core MD07-3088.

5. Results

5.1. Clay mineralogy

Clay mineralogy determination in core MD07-3088 displays the presence of 4 main clay types as reported in Fig. 3. The clay mineral assemblage shows a dominance of illite (20–60 %), smectite (10–50 %) and chlorite (30–50 %) with short-term amplitude fluctuations. Conversely, kaolinite (0–4 %) occurs in minor abundance .

The LGM period (22 to 18 ka) is characterized by the lowest contents of smectite ranging from 10 to 20 % except for one event between 19.7 and 19.4 ka BP when higher values of smectite until 30 % are recorded. In parallel, chlorite values display values ranging from 30 to 40 % with a maximum of 50 % between 19.7 and 19.4 ka BP. In contrast, during the LGM, illite contents show a

reverse trend, reaching highest amounts of 60 % between 21.4 and 20.5 ka BP followed by a two step decrease between 20.5 to 19.7 ka and 19.7 and 19.1 ka BP, the latter more marked until 20 %.

The LGIT (18 to 11.6 ka BP) clay pattern shows a two-step distribution. During the first part of the deglaciation (18 to 14.3 ka BP), smectite starts to increase from 10 to 50 %, well correlated to chlorite increasing from 30 to 40% whereas illite displays an opposite trend.

The second second step of the deglaciation, including the Antarctic Cold Reversal event from 14.3 to 12.7 ka BP is characterized by an abrupt decrease of smectite from 50 to 15 % whereas illite increases from 20 to 40 %. On the other hand chlorite does not show large variations ranging from 20 to 30%. These trends last longer until the end of LGIT (approximately 12 ka BP) before to reverse again since the onset of the Holocene (~11.6 to 10 ka).

Clay mineralogy obtained on the core MD07-3119 shows a similar distribution pattern since the last glacial/deglacial transition (Fig. 4). From 18.5 to 18 ka BP, smectite is characterized by low values of approximately 5 % except for a peak reaching 15 % at 18 ka BP, whereas lllite and chlorite show highest values of 45 % between 18.5 and 18.3 ka and 18 to 17 ka BP with a minimum recorded at 17.9 ka BP of 35 %. Since the first step of the deglacial period, between 17.7 and 14.4 ka BP, smectite starts to increase reaching 20 % and illite decreases until 30 %. By contrast, chlorite follows a slight increasing trend ranging between 40 % and 50 %. From 14.4 to 11.5 ka BP, smectite amount remains quite constant at 20 % similar to the chlorite and illite stable trend. During this time-span, ACR event is equally well marked as pointed out by a slight decrease of smectite between 14.3 and 13.7 ka BP.

Finally, the Early Holocene (11.6 to 10 ka BP) is characterized by a renewed increase of smectite reaching 27 % whereas illite and chlorite decrease until 25 % and 35 % respectively (Fig. 4).

5.2. Bulk geochemistry

Geochemical data by XRF scanning provides a semi-quantitative estimation of potassium (K), titanium (Ti) and zirconium (Zr) contents allowing deductions about the land derived material (Stuut et al., 2007).

K/Ti ratio and Zr recorded in core MD07-3088 are reported in Figure 5. The distributions of these elements clearly show important fluctuations during the last glacial compared to the LGIT and Early Holocene. Between 21.7 and 17.2 ka BP, K/Ti ratio displays highest values even though its general trend is punctuated by several short-term events marked by lower values of K/Ti ratio between 20.5 to 20 ka, 19.7 to 19.2 ka and 18.5 to 18.1 ka BP as previously suggested by Siani *et al.*, 2010 (Fig. 5). In parallel, Zr content also shows strong variability. Between 22 and 20 ka BP, Zr show an irregular pattern, with important alternation of lower and higher concentrations. The end of LGM is illustrated by low values of Zr even though a global increase is recorded. Between 18 and 16 ka, Zr amounts display maximum concentrations distributed through 4 major events dated at approximately 18, 17.6-17.5, 17.2 and 16.7 ka BP respectively. Finally, since the LGIT until the Early Holocene, the K/Ti

ratio and Zr content lie on a general decreasing trend reflecting a most likely change of the terrigeneous sources.

5.3. Grain-size

Grain-size results (clayey, silty, fine sandy and medium sandy classes as well as mean grain-size) of the core MD07-3088 are reported in Fig. 6. Sediment grain-size is dominated by silty fraction ranging from 80 to 90 % even though likewise important short-term fluctuations mark the LGM. From 22 to 18 ka BP, grain-size pattern is illustrated by at least 8 coarser events (> 63 μm) closely spaced in time at 21.1, 20.8, 20.5, 20, 19.6, 19.3, 18.5 and 18.2 ka respectively in agreement with maxima in the medium sandy fraction (> 100 μm) and the mean grain-size. During the first step of the deglaciation, between 18 and 15 ka, 5 isolated coarser peaks reaching 20 % were recovered at approximately 17.6, 17.4, 17.1,16.7 and 15.3 ka. Then, from 14.5 to 13.2 ka BP, mean grain-size tends to increase again from 15 to 28 % reaching maxima during the ACR interval marked by at least three main coarser events. Finally, a subsequent grain-size decline at 15 % was observed between 12.7 and 11.5 ka BP even though marked by a coarser event at ~12.2 ka. Finally, the Early Holocene (11.5 to 10 ka BP) is characterized by one distinct coarser episode centred at 10.7 ka.

Grain-size analyses obtained for the MD07-3119 core display low variability of clays, silts and sandy contents with short term variability within each fraction (Fig. 7). During the last glacial period, coarser fraction is more pronounced from 18.5 until 17.5 ka. The first deglacial rise is characterized by two slightly higher grain-size events at 17.2 and 15.7 ka respectively. A significant decrease in the mean grain-size at 14.4 ka is recorded corresponding to the onset of the ACR event in core MD07-3088, which is reversely marked by several short-term coarser events until about 12.8 ka (Fig. 6). Finally, a progressive increase in the mean grain-size was observed until the Early Holocene punctuated by one slightly coarser events at 11.3 ka.

6. Interpretation and discussion

6.1. Terrigenous inputs provenance

Clay mineralogy variability of surface sediments in the southern Chile does not match variations in lithology or diagenesis and may likely derive from primarily detrital sources (Stuut et al., 2007; Siani et al., 2010). Our assumption is corroborated by the fact that abundance peaks of smectite are not correlated with abundance peaks of volcanic glass shards identified in the core MD07-3088 (Carel et al., 2011). We can thus consider that smectite derives from sedimentary processes and not from the alteration of volcanic products by hydrothermal processes on the sea floor.

The clay mineralogy of various South Chilean sites has been studied in several marine cores (Lamy et al., 1999, 2001; Marinoni et al., 2008). In general, sediments between 25°S to 45°S show a

decreasing trend of smectite content characterized by a north to south gradient, mainly attributed to the variety of source rocks (Lamy et al., 1998; Stuut et al., 2007). Northernmost to our regional context, clay mineralogical studies based on surface samples exhibit generally high smectite contents followed by chlorite and illite (Lamy et al., 2001; Stuut et al., 2007). These results confirm that the clay mineralogical assemblage in sediments of the south Chilean margin is mainly transported from the surrounding continental rocks to the studied site by river and/or glacier dynamic. In addition, we cannot neglect that a significant contribution of sediment can be transported to the studied site through ocean currents. Finally, a major aeolian contribution can be discarded due to prevailing westerly winds and high sedimentation rates in our study site.

Therefore, the identification of the potential clay source and the transport processes of sedimentary material and their changes in the past are required to provide a paleoclimatic interpretation. Continental hinterland is formed by Paleozoïc basement and low-grade metamorphic rocks of the Coastal Range composed essentially by potassium-rich plutonic rocks, by igneous rocks of the Patagonian Batholith and the titanium-rich volcanic products of the Andean Cordillera (Stern, 1984; Zeil, 1986; Corgne et al., 2001). At high latitudes, illite is a primarily mineral and derive from the alteration of the phyllosilicates contained in granitoids (Chamley, 1989) and represents the physical erosion of metamorphic and plutonic rocks of the Coastal Range. In opposite, smectite formation results from chemical weathering of Ti-rich volcanic products composing the Andean Cordillera (Forsythe et al., 1986; Futa and Stern, 1988).

As a consequence, the K/Ti ratio as well as the smectite/illite ratio can be used as proxy to distinguish sources contributions, either from the Coastal Range and the Andean Cordillera. Comparison between smectite/illite and K/Ti ratios is illustrated in Fig. 8 and clearly shows an anti-correlated behaviour of these two proxies. Lowest values (≈0.3) of smectite/illite punctuated the last glacial and the beginning of the deglacial period between 21.4 to 17.3 ka and are associated to highest values of K/Ti (from 2.5 to 3). However, a short-term reversal trend was observed between 19.7 and 19.2 ka BP when smectite/illite ratio increases until 1 associated to lower values of K/Ti (Fig. 8). These observations suggest that the source of detrital inputs during the last glacial is mainly controlled by K-rich Coastal Range physical erosion in agreement with previous observations of a maximal extension of the Patagonian icefields during the last glacial (Heusser, 2002; Glasser et al., 2004), explaining the exclusive contribution of the Coastal Range owing to the growth of icefields preventing the weathering of subjacent Andean products. On the other hand, the 19.7-19.2 ka interval seems to be more characterized by Andean Cordillera contribution suggesting a short-term retreat phase of the northern Patagonian icecap. This hypothesis is corroborated by the coeval increase of chlorite that could reflect the input of plutonic ice-free suite, which includes the Cabo Raper and Seno Hoppner plutons located in the most western portion of the peninsula of Taitao (Bourgois et al., 2000).

The Smectite/illite ratio starts to increase at 17.2 ka BP coeval to an abrupt decrease of the K/Ti ratio. These conditions persist until 14.2 ka BP illustrating the deglacial warming as also indicated by the SST record and the coeval decreasing trend of the stable oxygen isotopic signal in core MD07-3088

(Fig.10). This warming could have favoured the progressive calving of icecaps exposing Andean volcanic products, which in turn have been more easily transferred to our study site. The following ACR interval (14.2 to 12.7 ka BP) is marked by a renewed glacial activity as illustrated by the SST cooling and by an abrupt decrease of smectite/illite ratio as well as by a slight increase of K/Ti ratio. During this cooling period, a probable glacier re-advances emphasizes the increased contribution of the Coastal Range products.

Finally since 12.7 ka BP, warming conditions prevail until 10 ka BP with a clear dominance of Andean Cordillera sediment provenance.

6.2. Evidences of ice-rafetd detritus and icecap fluctuations since the LGM

Directly dependant of glaciers ablation, the occurrence of ice-rafted debris (IRD) is particularly difficult to assess because of the distinction between ice-rafted and coarse particles is relatively thin. Identification of IRD events is invaluable to translate glaciers fluctuations because of the flux of IRD is expected to correlate with the discharge of icebergs to open marine environments (Weltje and Prins, 2003). In glaciated regions, particles sizes are controlled by two major deposits modes: glacial grinding and/or IRD (Reimnitz et al., 1998). Glacial grinding is characterized by continuous series of grain-size whereas IRD are typically transported in mass and display a wide range of discontinuous grain-sizes from clay to gravel (Weltje and Prins, 2003). To determine a possible existence of IRD, a further sampling every 5 mm over 5 cm on both sides of the two major observed coarser peaks (1368 cm, 19.2 ka BP and 1558 cm, 19.6 ka BP respectively; Fig. 9) has been performed in core MD07-3088. Refined grain-size pattern clearly show a bi-modal distribution characterizing IRD deposits as already suggested by Weltje and Prins (2003). These two layers have been deposited during the LGM, we can thus hypothesize that higher values of medium sandy fraction as well as higher mean grain-size could probably result from IRD events mainly driven by massive iceberg discharges. This result is also supported by SEM imaging of coarse particles handpicked in these two layers, which illustrate the typical IRD shape pointing out jagged and fractured particles and/or blunted forms more or less pronounced as a function of the haulage intensity (Fig. 9). Finally, the diminishing of the coarser fraction proportion in core MD07-3119, located westward the MD07-3088 site in an open ocean setting and therefore much less affected by direct continental supply, could imply the hypothesis of the minor contribution of oceanic current circulation-linked sediment inputs (Fig. 7 and 10).

The presence of IRD in core MD07-3088 is thus a robust support to quantify icecaps. Recurrence of IRD is recorded during the last glacial through abundant peaks of the medium sandy fraction (> 100 μm; Fig. 9). During the last glacial, grain-size observations are supported by Zr distribution, used as a proxy of the closeness of the source. Recent studies from the neighboring fjord of Golfo Elefantes suggested that Zr is particularly sensitive in proximal environments because it is strongly associated to heavy/coarser fractions as oxides (Bertrand et al. 2012). During the last glacial

period (21.5 to 18 ka BP), identified IRD events are concordant with higher values of Zr. Major peaks in medium sandy fraction recorded at 21.1, 20.8, 20.5 and between 19.7 to 18.2 ka BP correspond to Zr enrichment in bulk sediments centred at approximately 21.3, 20.6, 19.6, 18.5 and 18.2 ka BP respectively. The hypothesis of the association between Zr and coarse particles in inner fjords evoked by Bertrand et al. (2012) is thus equally verified in proximal marine environments. The general coarse grain-size recorded during the last glacial is also supported by the high content of illite in the sediments suggesting an important discharge by glaciers via the fjords system and from a proximal Coastal Range source.

In addition, the fluctuation in the magnetic properties shows a similar behaviour (Fig. 9). ARM directly responds to the concentration and grain-size variations and is preferentially carried by finer particles, due to its sensitivity to variations in the fined-grain fractions (Weeks et al., 1993; Kissel, 2005). As a consequence, we can determine the ARM/IRM ratio that can be used to illustrate the magnetic susceptibility of the finer size fraction. The ARM/IRM ratio decreasing is generally attributed to a higher proportion of coarser particles. Figure 9 displays the distribution of this ratio indicating a large variability along the core, with lower values between 22 and 18 ka BP concordant with high proportions of coarse populations except for the interval between 20 and 19.7 ka BP.

The Termination I (18 to 10 ka BP) is on the contrary characterized by a continuous decrease trend of Zr, associated to finer mean grain-size except for three major intervals between 18 and 16.3 ka, 14.2 to 12.7 ka and 10.6 to 10.4 ka BP. These reverse trends mark important changes in the transport dynamic and a more distant source. Constant diminishing of Zr amounts and relatively finer grain-size suggest a prevailing fluviatile transport via pro-glacial rivers network and a more distal source, as previously observed with the increasing smectite trend originating from the more distal Andean Cordillera. In parallel, the ARM/IRM ratio slightly increases and remains constant from 18 to 10 ka in accordance with higher proportion of fine particles typical of fluviatile transport. Finally the ACR episode is equally evidenced with an abrupt decrease of ARM/IRM ratio between 14.2 and 12.7 ka BP, when renewed glacial activity is recorded.

6.3. Paleoclimatic implications

Combination of continental source changes and IRD events since the LGM may decipher climate variability at high southern latitudes of southern Patagonia. Exclusive control of illite in clay assemblages and recurrent IRD features during the LGM hypothesize prevailing cold climatic conditions in southern Patagonia between 22 and 18 ka BP, marked by the northern icecap extension favouring erosion of proximal Coastal Range and important icebergs discharge. These findings are in accordance with the SST record that evidences lowest temperatures of approximately 10 °C at 46°S during this time span (Fig. 10). Cooling was equally recorded at higher latitudes in the Strait of Magellan (53°S) from the deep-sea MD07-3128 record (52°65’S, 75°56’W, 1,032 m bsl) and estimated from alkenones-derived SST at approximately 4-6°C compared to modern ones (Caniúpan

et al., 2011). These authors showed also the presence of IRD events during the LGM with two major peaks dated approximately between 21.2 and 21 ka BP and between 20.3 and 20 ka BP. Compared to our record, which shows IRD events between 21 and 20.5 ka BP and 19.7 and 19.4 ka BP respectively, we assume that this discrepancy, associated to general cold conditions at 46°S is strongly linked to the northward migration and strengthening of the SWW cell as previously evoked by Lamy et al., 1999 with a northward shift of 5-6° compared to its modern position of 50-55°S (Kaiser et al., 2005) could probably explain the staggered response between the northern and southern icecaps. Such scenario implies maximum snow accumulation over mid-latitudes southern Andean reliefs between 21 and 20.5 ka BP and between 19.7 and 19.4 ka BP as suggested by grain-size patterns. These glacial advances are coeval with previous glaciological studies performed on moraines fronts in Bahia Inutil (53°S) that evidenced 2 major extension phases dated between 22 and 20.5 ka BP and between 19 and 17.5 ka BP respectively (McCulloch et al., 2005). Superimposed on this general cold trend, the large amplitude of grain-size fluctuations and the record of the warmer event between 20 and 19.3 ka BP, marked by smectite increase suggesting a rapid short-scale response of the northern Patagonian icecap behaviour to climate forcing.

The Termination I starts to settle at approximately 18 ka BP and is characterized by short-scale alternations of successive warming and cooling phases continuing until 10 ka BP. Persisting cold conditions between 18 and 17 ka BP are abruptly disrupted at 17 ka BP by the settlement of optimal conditions with emphasized predominant smectite-derived andean source contribution by fluviatile inputs, outright recorded in the core MD07-3088 but slightly later in the open ocean. Progressive warming setting up is conspicuous with increase SST (Siani et al., 2012) and uninterrupted decreasing precipitations and thus snow accumulation (Montade et al., 2012) at the same latitude supported warmer and drier conditions resulting from southward migration of SWW leading Andean reliefs calving (Wingenter et al., 2010). Resulting evidences of SST increase at 46°S during this time span is synchronous with the global warming recorded in the whole Southern Ocean (Wolff et al., 2006) and tentatively attributed to the Mystery Interval between 17.5 and 14.9 ka BP (Denton et al., 2006) according to the dating uncertainties. Global warming is interrupted by a renewed glacial activity between 14.3 and 12.7 ka BP, consistent with $\delta^{18}O$ reconstructions (Fig. 6) and attributed to the Antarctic Cold Reversal event. Event though the geographic and temporal extension of this cooling episode remains still debated, northern Patagonian icecap glacier advances evidenced by abundant pulses of IRD and drastic changes in the source contributor match well with synchronous southern icecap extension ranging from 14.8 and 11.8 ka BP at Torres del Paine (51°S; Moreno et al., 2009), dated between 14.8 and 11.8 ka BP from moraines ice lobes of Ultima Esperanza (52°S; Sagredo et al., 2011) and at larger time-scale between 15.5 and 11.8 ka BP in the Strait of Magellan (53°S; McCulloch et al., 2005). The postulation of the large extension prevailing colder conditions in the whole southern hemisphere is strongly supported by glacial re-advance in New Zealand Southern Alps on the eastern coast of south Pacific between 14.6 and 12.8 ka BP (Putnam et al., 2010). The only probable explanation of the northward migration of the SWW in this case is controversial as suggested

by SST and pollen records, which predict enhanced warm and dry conditions (Fig. 10). As a consequence, glacial activity during ACR seems to be more probably driven by internal ice dynamic control above climate forcing. ACR ceased from 12.7 ka BP, when a return to warmer conditions is interpreted according to steady increasing of SST linked to resumption of smectite contribution in detrital supplies mineralogy. The general fine grain-size testifies of an intense glacier recession and important supplies of fluviatile-carried silty material resulting from densification of drainage areas. Nonetheless, during Early Holocene (11.5 to 10 ka BP), two smaller amplitude cooler events are superimposed on the global warming trend and estimated between approximately 11.7 and 11.3 ka BP and 10.6 and 10.4 ka BP respectively. Despite the long-term settlement of optimal conditions, this cooled punctuations could correspond to Early Holocene glacier readvances identified from cosmogenic nuclides surface exposure from moraines of glacier Exploradores (Rio Bayo Valley) between 12.5 ± 0.9 and 10.5 ± 0.8 ka BP and between 10.7 and 9.7 ka BP respectively (Glasser et al., 2004; 2006).

7. Conclusion

Sedimentological defined proxies (clay mineralogy and grain-size) and evidenced dated glacier advances are excellent markers to point out the major role of SWW to explain climate variability at high Southern latitudes.

Mineralogical and grain-size evidences suggest that icecap extension was at the height during the LGM (22-18 ka BP) punctuated by short-term fluctuations, with high recurrence of IRD events and an exclusive contribution of the proximal Coastal Range in the detrital supplies. At least 4 episodes of glaciers advances are recorded at 21.1, 20.7, 20.5 and between 19.7 and 19.2 ka BP coeval with the historical advances identified at southernmost latitudes.

The Termination I (18 to 14.2 ka BP) is characterized by alternation between warmer and cooler events. After cooling episodes between 18 and 17 ka BP in continuity of the last glacial, warming settled from 17 to 14.3 ka BP as evidenced by increasing SST estimated at approximately 4-5 °C, increasing amount of smectite and decreasing rainfalls inducing intense glacial recession. This event, concordant with the “Mystery Interval” is abruptly disrupted by a return to glacial conditions recorded between 14.3 and 2.7 ka BP coeval with the Antarctic Cold Reversal as illustrated by decreasing trend of the smectite/illite ratio and a renewed abundance of IRD events emphasizing the idea of the northern icecap extension, correlated with historical southernmost glacier advances. Afresh warming is recorded since 12.7 ka BP, persisting until Early Holocene marked by high SST and smectite amounts in clay assemblage suggesting icecap retreat and finer grain-size inducing by fluviatile transport vector.

The most plausible explanation of such findings resides in the latitudinal migration of the SWW cell, which migrates northernwards and strengthens during cooler events inducing intense snow accumulation over Andean reliefs preventing weathering of smectite-derived volcanic rocks as evoked

to explain cooling during LGM and ACR episodes. Glacial retreat recorded during “Mystery Interval” and Early Holocene caused by southward migration of SWW favour the production of smectite and the development of fluviatile network that finer drains finer material.

Nevertheless, even though SWW migration seems to be a robust basis to explain southern latitudes climate variability, others parameters like internal ice dynamics must to be taken into account and further studies focused on oceanic circulation will allow to better understand the interconnection between SWW circulation and atmospheric features.

References

Aniya, M., Sato, H., 1995. Holocene glacial chronology of Upsala Glacier at Peninsula Herminita, Southern Patagonia Icefield. Glacier research in Patagonia. *Bulletin of Glacier Research* 13, 83–96.

Aniya, M., Enomoto, H., 1986. Glacier variations and their causes in the Northern Patagonian Icefield, Chile since 1944. *Arctic and Alpine Research* 18, 307–316.

Bertrand, S., Hughen, K.A., Sepúlveda, J., Pantoja, S., 2012. Geochemistry of surface sediments from the fjords of Northern Chilean Patagonia (44–47°S) : Spatial variability and implications for paleoclimate reconstructions. *Geochimica et Cosmochimica Acta* 76, 125–146.

Bourgois, J., Guivel, C., Lagabrielle, Y., Calmus, T., Boulègue, J., Daux, V., 2000. Glacial-interglacial trench supply variation, spreading-ridge subduction, and feedback controls on the Andean margin development at the Chile triple junction area (45–48°S). *Journal of Geophysical Research* 105, 8355–8386.

Brandhorst, N.V., 1971.Condiciones oceanográficas estivales frente a la costa de Chile. *Revista de Biología Uarina*. *Valparaíso* 14, 45–84.

Bronk-Ramsey, C., 2009. Bayesian analysis of radiocarbon dates. *Radiocarbon* 51, 337–360.

Cande, S.C., Leslie, R.B., 1986. Late Cenozoic Tectonics of the Southern Chile Trench. *Journal of Geophysical Research*, vol., 91, no. B1, 471–496.

Caniupan, M., Lamy, F., Lange, C.B., Kaiser, J., Arz, H., Kilian, R., Baeza Urrea, O., Aracena, C., Hebbeln, D., Kissel, C., Laj, C., Mollenhauer, G., Tiedemann, R., 2011. Millennial-scale sea surface temperature and Patagonian Ice Sheet changes off southernmost Chile (53°S) over the past ~60 kyr. *Paleoceanography* 26, PA3221, 1–10.

Carel, M., Siani, G., Delpech, G., 2011. Tephrostratigraphy of a deep-sea sediment sequence off the south Chilean margin : New insight into the Hudson volcanic activity since the last glacial period. *Journal of Volcanology and geothermal Research* 208, 99–111.

Chamley, H., 1989. Clay Sedimentology Springer, Berlin, 623 pp.

Coplen, T.B., 1988. Normalization of oxygen and hydrogen isotope data. *Chemical Geology* 72, 293–297.

Corgne, A., Maury, R.C., Lagabrielle, Y., Bourgois, J., Suarez, M., Cotten, J., Bellon, H., 2001. La

diversité des basaltes de Patagonie à la latitude du point triple du Chili (46°–47° lat. S): données complémentaires et implications sur les conditions de la subduction. *Comptes Rendus de l'Académie des Sciences, Paris, Sciences de la terre et des Planètes* 333, 363–371.

Denton, G., Broecker, W.S., Alley, R.B., 2006. The mystery interval 17,5 to 14,5 kys ago. *PAGES News* 2, 14–16.

Denton, G., Karlén, W., 1973. Holocene climatic variations – Their pattern and possible causes. *Quaternary Research* 3, 155–205.

Douglass, D.C., Singer, B.S., Kaplan, M.R., Mickelson, D.M., Caffee, M.W., 2006. Cosmogenic nuclide surface exposure dating of boulders on last-glacial and late-glacial moraines, Lago Buenos Aires, Argentina: Interpretive strategies and paleoclimate implications. *Quaternary Geochronology* 1, 43–58.

Douglass, D.C., Singer, B.S., Kaplan, M.R., Ackert, R.P., Mickelson, D.M., Caffee, M.W., 2005. Evidence of early Holocene glacial advances in southern South America from cosmogenic surface-exposure dating. *Geology*, vol. 33, no. 3, 237–240.

Duplessy, J.C., 1978. Isotope studies. In: Gribbin, J. (eds), Climatic Changes. Cambridge University Press, Cambridge, pp. 46–67.

Folk, R. L., Ward,W. C., 1957. Brazos river bar: a study in the signifiance of grain size parameters, *Journal of Sedimentary and Petrology* 27, 3–26.

Forsythe, R.D., Nelson, E.P., Carr, M.J., Kaeding, M.E., Hervé, M., Mpodozis, C.M., Soffia, M.J., Harambour, S., 1986. Pliocene near trench magmatism in southern Chile: A possible manifestation of ridge collision. Geology 14, 23–27.

Fujiyoshi, Y., Kondo, H., Inoue, J., Yamada, T., 1987. Characteristics of precipitation and vertical structure of air temperature in Northern Patagonia. *Bulletin of Glacier Research* 4, 15–24.

Futa, K., Stern, C.R., 1988. Sr and Nd isotopic and trace element compositions of Quaternary volcanic centers of the southern Andes. *Earth and Planetary Science Letters* 88, 253–262.

Garreaud, R.D., Aceituno, P., 2007. Atmospheric circulation and climatic variability. *In : The physical geography of South America*. Ed. by Veblen, T., Young, K., Orme, A. New York, Oxford University Press, 45–59.

Glasser, N.F., Jansson, K.N., Harrison, S., Kleman, J., 2008. The glacial geomorphology and Pleistocene history of South America between 38°S and 56°S. Quaternary Science Reviews, vol. 27, issues 3–4, 365–390.

Glasser, N.F., Harrison, S., Ivy-Ochs, S., Duller, G.A.T., Kubik, P., 2006. Evidence from the Rio Bayo valley on the extent of the North Patagonian Icefield during the Late Pleistocene–Holocene transition. *Quaternary Research* 65, 70–77.

Glasser, N.F., Harrison, S., Winchester, V., Aniya, M., 2004. Late Pleistocene and Holocene palaeoclimate and glacier fluctuations in Patagonia. *Global and Planetary Change* 43, 79–101.

Haberle, S.G., Lumley, S.H., 1998. Age and origin of tephras recorded in postglacial lake sediments to

the west of the southern Andes, 44°S to 47°S. *Journal of Volcanology and Geothermal Research* 84, 239–256.

Heusser, C.J., 2002. On glaciation of the Southern Andes with special reference to the Peninsula de Taitao and adjacent Andean cordillera (~46°30'). *Journal of South American Earth Sciences* 15, 577 – 589.

Heusser, C.J., 1993. Late-glacial of southern South America. *Quaternary Science Reviews* 12, 345–350.

Hulton N.R.J., Purves R.S., McCulloch R.D., Sugden D.E., Bentley, M.J., 2002. The Last Glacial Maximum and deglaciation in Southern South America. *Quaternary Science Rev*iews 21, 233-241.

Kaiser, J., Lamy, F., Hebbeln, D., 2005. A 70-kyr sea surface température record off Southern Chile. *Paleoceanography* 20, PA4009, pp. 15.

Kaplan, M.R., Fogwill, C.J., Sudgen, D.E., Hulton, N.R.J., Kubik, P.W., Freeman, S.P.H.T., 2008. Southern Patagonian glacial chronology for the Last Glacial period and implications for Southern Ocean climate. *Quaternary Science Reviews* 27, 284–294.

Kaplan, M.R., Ackert, R.P., Singer, B.S., Douglass, D.C., Kurz, M.D., 2005. Cosmogenic nuclide chronology of millenial-scale glacial advances during O-isotope Stage 2 in Patagonia. *Bulletin of Geological Society of America* 116, 308–321.

Kissel, C., 2005. Magnetic signature of rapid climatic variations in glacial North Atlantic, a review. External Geophysics, Climate and Environment (Climate), *C.R. Geoscience* 337, 908–918.

Kissel, C., 2007. The shipboard Scientific party, MD159-PACHIDERME-IMAGES XV, cruise report. *Les rapports de campagne à la mer*. Institut Paul-Emile Victor, pp. 105.

Lamy, F., Hebbeln, D., Röhl, U., Wefer, G., 2001. Holocene rainfall variability in southern Chile: a marine record of latitudinal shifts of the Southern Westerlies. *Earth and Planetary Science Letters* 185, 369–382.

Lamy, F., Hebbeln, D., Wefer, D., 1999. Marine record of climatic change in mid-latitude Chile during the last 28,000 years based on terrigenous sediment parameters. *Quaternary Research* 51, 83–93.

Lamy, F., Hebbeln, D., Wefer, G., 1998. Late Quaternary precessional cycles of terrigenous sediment input off the Norte Chico, Chile (27.5ºS) and palaeoclimatic implications. *Palaeogeography, Palaeoclimatology, Palaeoecology* 141, 233–251.

Marinoni, L., Setti, M., Salvi, C., López-Galindo, A., 2008. Clay minerals in late Quaternary sediments from the south Chilean margin as indicators of provenance and palaeoclimate. *Clay Minerals* 43, 235–253.

McCulloch, R.D., Bentley, M.J., Tipping, R.M., Clapperton, C.M., 2005. Evidence for late-glacial ice dammed lakes in the central Strait of Magellan and Bahía Inútil, southernmost South America. *Geografiska Annaler*, Series A-Physical Geography 87, 335–362.

Miller A., 1976. The climate of Chile. *In : World Survey of Climatology*, ed. Schwerdtfeger, W.,

Elsevier, Amsterdam. pp. 107–134.

Minster, J.B., Jordan, T.H., Molnar, P., Haines, E., 1974. Numerical Modelling of Instantaneous Plate Tectonics. *Geophysical Journal of the Royal Astronomical Society* 36, 541–576.

Montade, V., Combourieu Nebout, N., Chapron, E., Mulsow, S., Abarzúa, A.M., Debret, M., Foucher, A., Desmet, M., Winiarski, T., Kissel, C., 2012. Regional vegetation and climate changes during the last 13 kyr from a marine pollen record in Seno Reloncaví, Southern Chile. *Review of Palaeobotany and Palynology* 181, 11 – 21.

Moore, D.M., Reynolds, R.C., 1989. X-ray Diffraction and the Identification and Analysis of Clay Minerals. New York Oxford University Press, pp. 332.

Moreno, P.I., Kaplan, M.R., François, J.P., Villa-Martinez, R.P., Moy, C.M., Stern, C.R., Kubik, P.W., 2009. Renewed glacial activity during the Antarctic cold reversal and persistence of cold conditions until 11.5 ka in southwestern Patagonia. *Geology* 37, 375–378.

Naranjo, J.A., Stern, C.R., 1998. Holocene explosive activity of Hudson Volcano, southern Andes. *Bulletin of Volcanology* 59, 291–306.

Petschick, R., Kuhn, G., Gingele, F., 1996. Clay mineral distribution in surface sediments of the South Atlantic: sources, transport and relation to oceanography. *Marine Geology* 130, 203–229.

Putnam, A.E., Schaefer, J.M., Barrell, D.J.A., Vandergoes, M., Denton, G.H., Kaplan, M.R., Finkel, R.C., Schwartz, R., Goehring, B.M., Kelley, S.E., 2010. In situ cosmogenic 10Be production-rate calibration from the Southern Alps, New Zealand. *Quaternary Geochronology* 5, 392–409.

Reimer, P.J., Baillie, M.G.L., Bard, E., Bayliss, A., Beck, J.W., Blackwell, P.G., Ramsey, C.B., Buck, C.E., Burr, G.S., Edwards, R.L., Friedrich, M., Grootes, P.M., Guilderson, T.P., Hajdas, I., Heaton, T.J., Hogg, A.G., Hughen, K.A., Kaiser, K.F., Kromer, B., McCormac, F.G., Manning, S.W., Reimer, R.W., Richards, D.A., Southon, J.R., Talamo, S., Turney, C.S.M., van der Plicht, J., Weyhenmeye, C.E., 2009. Intcal09 and Marine09 radiocarbon age calibration curves, 0–50,000 years cal BP. *Radiocarbon* 51, 1111–1150.

Reimnitz, E., McCormick, M., Bischof, J., Darby, D.A., 1998. Comparing sea-ice sediment load with Beaufort Sea shelf sediments: is entrainment selective? *Journal of Sedimentary Research* 68, 777–787.

Richter, T.O., Van der Gaast, S., Koster, B., Vaars, A., Gieles, R., De Stigter, H., De Haas, H.,van Weering, T.C.E., 2006. The Avaatech XRF core scanner: technical description and applications to NE Atlantic sediments. In: Rothwell, R.G. (Ed.), *New Techniques in Sediment Core Analysis*. Special Publication, vol. 267. Geological Society, London, 39–50.

Roth, H., Stuefer, M., Siegel, A., Skvarca, P., Eckstaller, A., 1998. Mass fluxes and dynamics of Moreno Glacier, Southern Patagonian Icefield. *Geophysical Research Letters* 25, 1407–1410.

Sagredo, E.A., Moreno, P.I., Villa-Martinez, R., Kaplan, M.R., Kubik, P.W., Stern, C.R., 2011. Fluctuations of the Ùltima Esperanza ice lobe (52°S), Chilean Patagonia, during the last glacial maximum and termination 1. *Geomorphology* 125, 92–108.

Sandgren, P., Snowball, I., 2001. Application of mineral magnetic techniques to Paleolimnology, In. Tracking environmental change using lake sediments, vol. 2. *Kluwer Academic Publishers*, 217–237.

Siani, G., Michel, E., De Pol-Holz, R., Lamy, F., Carel, M., Lourantou, A., 2012. Southern Ocean deglacial reservoir age changes and timing of three episodes of upwelling. *Submitted à Science*.

Siani G., Colin C., Michel E., Carel M., Richter T., Kissel C., Dewilde F., 2010. Late Glacial to Holocene terrigenous sediment record in the Northern Patagonian margin: Paleoclimate implications. *Palaeogeography, Palaeoclimatology, Palaeoecology* 297 (1), 26–36.

Stern, C.R., Futa, K., Muehlenbachs, K., 1984. Isotope and trace element data for orogenic andersites in the Austral Andes. In: Harmon, R.S., Barreirro, B.A. (Eds.), *Andean magmatism: chemical and isotopic constraints*. Shiva Press, Cheshire, England, 31–46.

Strub P.T., Mesias J.M., Montecino V., Ruttlant J., Salinas S., 1998. Coastal ocean circulation off Western South America. In The Global Coastal Ocean. *Regional Studies and Syntheses (eds Robinson, A.R., Brink, K.H.)*, Wiley, New York. pp. 273–315.

Stuut, J-B. W., Kasten, S., Lamy, F., Hebbeln, D., 2007. Sources and modes of terrigenous sediment input to the Chilean continental slope. *Quaternary International* 161, 67–76.

Trenberth, K.E., 1991. Climate Diagnostics from Global Analyses: Conservation of Mass in ECMWF Analyses. *American Meteorological Society*, vol. 4, 707–722.

Trentesaux, A., Recourt, P., Bout-Roumazeilles, V., Tribovillard, N., 2001. Carbonate grain-size distribution in hemipelagic sediments from a laser particle sizer. *Journal of Sedimentary Research*, Special Paper, vol. 71, no. 5, 858–862.

Weeks, R., Laj, C., Endignoux, L., Mazaud, A., Labeyrie, L., Roberts, A., Kissel, C., Blanchard, E., 1995. Normalised natural remanent magnetisation intensity during the last 240 000 years in piston cores from the Central North Atlantic Ocean: geomagnetic field intensity or environmental signal? *Physical Earth and Planetary International* 87, 213–229.

Weeks, R., Laj, C., Endignoux, L., Fuller, M., Roberts, A., Manganne, R., Blanchard, E., Goree, W., 1993. Improvements in long-core measurement techniques: applications in paleomagnetism and palaeoceanography. *Geophysical Journal International* 11, 651–662.

Weltje, G.J., Prins, M.A., 2003. Muddled or mixed? Inferring paleoclimate from size distributions of deep-sea clastics. *Sedimentary Geology* 162, 39–62.

Wenzens, G., 2001. Comment : Climatic inferences from glacial palaeoecological evidence at the last glacial termination, Southern South America. *Journal of Quaternary Science* 16, 291–293.

Wingenter, O.W., Elliott, S.M., Blake, D.R., 2010. New Directions: Restoring the westerly winds in the southern Hemisphere: Climate's lever. *Atmospheric Environment* 44, 3866–3868.

Wolff, E.W., Fischer, H., Fundel, F., Ruth, U., Twarloh, B., Littot, G.C., Mulvaney, R., Rothlisberger, R., de Angelis, M., Boutron, C.F., Hansson, M., Jonsell, U., Hutterli, M.A., Lambert, F., Kaufmann, P., Stauffer, B., Stocker, T.F., Steffensen, J.P., Bigler, M., Siggaard-Andersen,

M.L., Udisti, R., Becagli, S., Castellano, E., Severi, M., Wagenbach, D., barbante, C., Gabrielli, P., Gaspari, V., 2006. Southern Ocean sea-ice extent, productivity and iron flux over the past eight glacial cycles. *Nature* 449, 748–758.

Wyrwoll, K.H., Dong, B., Valdes, P., 2000. On the position of southern hemiphere westerlies at the Last Glacial Maximum: an outline of AGCM simulation results and evaluation of their implications. *Quaternary Science Reviews* 19, 881–898.

Zeil, W., 1986. “Südamerika.” Enke Verlag, Stuttgart.

FIGURES AND TABLES:

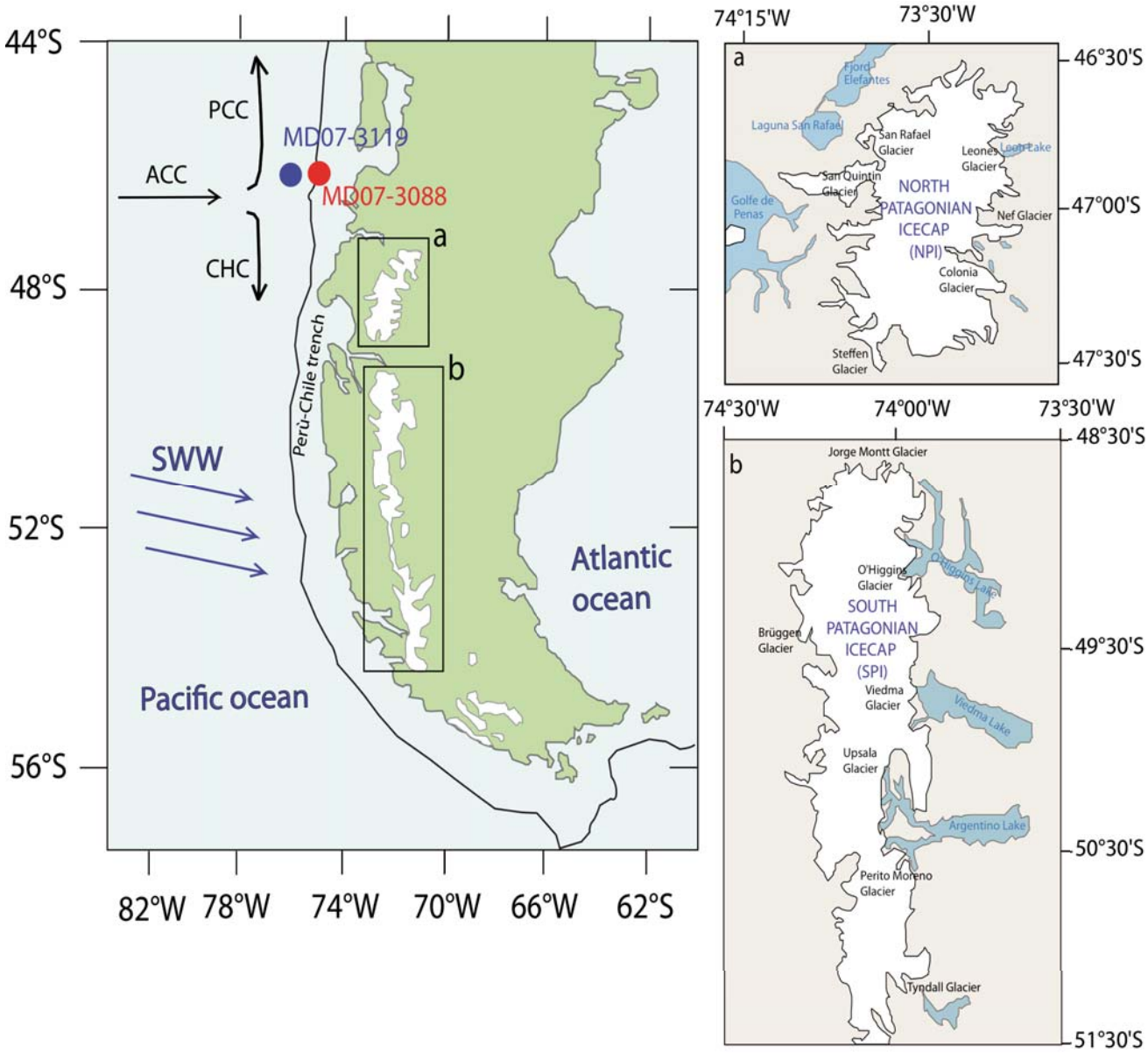

Figure 1: Map of the Southern Patagonia with climatic features (SWW: Southern Westerly Winds and major currents: ACC, Antarctic Circumpolar current, PCC: Peru-Chile current, CHC: Cap Horn current). Modern location of the two active patagonian icecaps and position of the deep-sea cores MD07-3088 and MD07-3119; Inserts show morphologies of each icecap (a) NPI and (b) SPI with associated glaciers tongues and drainage areas

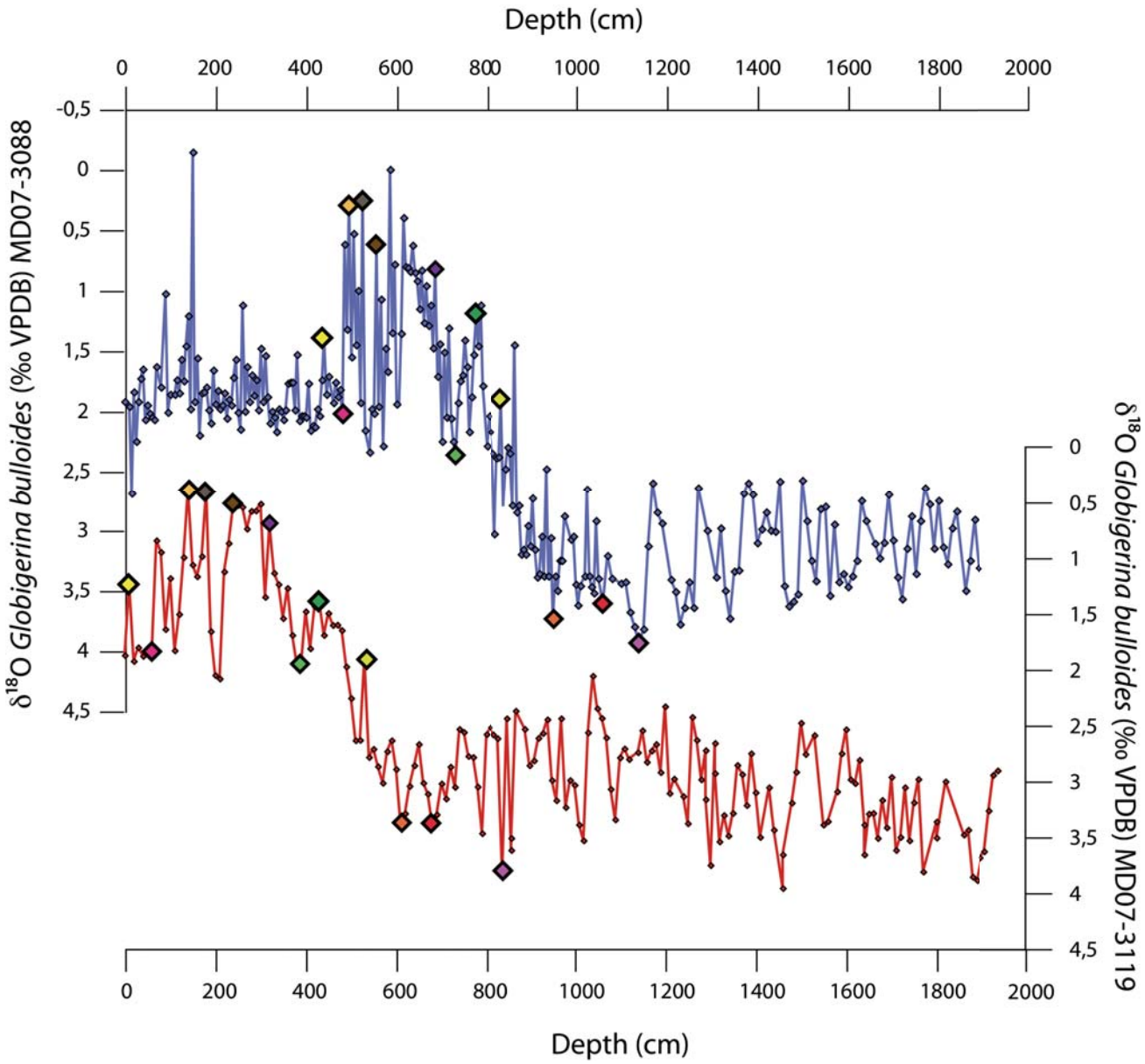

Figure 2: Depth correlations between the oxygen isotope records from the deep-sea cores MD07-3088 and MD07-3119. Diamonds correspond to the tie-points obtained for core MD07-3119.

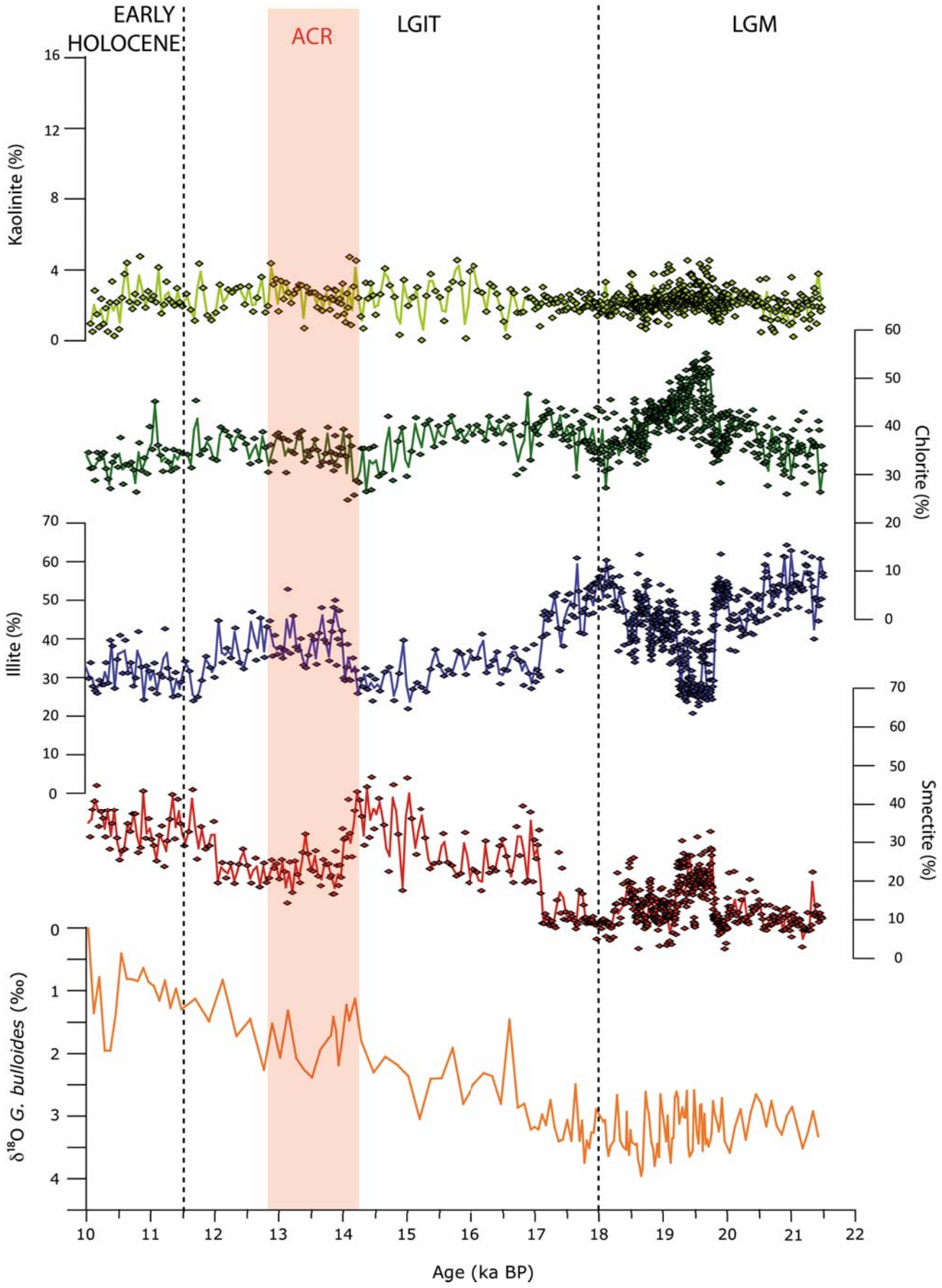

Figure 3: Distribution of the four main clay types of the core MD07-3088 as a function of time during the last glacial to deglacial period (22 to 10 ka BP) compared to the $\delta^{18}O$ record obtained from the planktonic foraminifera *Globigerina bulloides*
LGM: Last glacial maximum; LGIT: Last glacial-interglacial transition; ACR: Antarctic Cold Reversal event

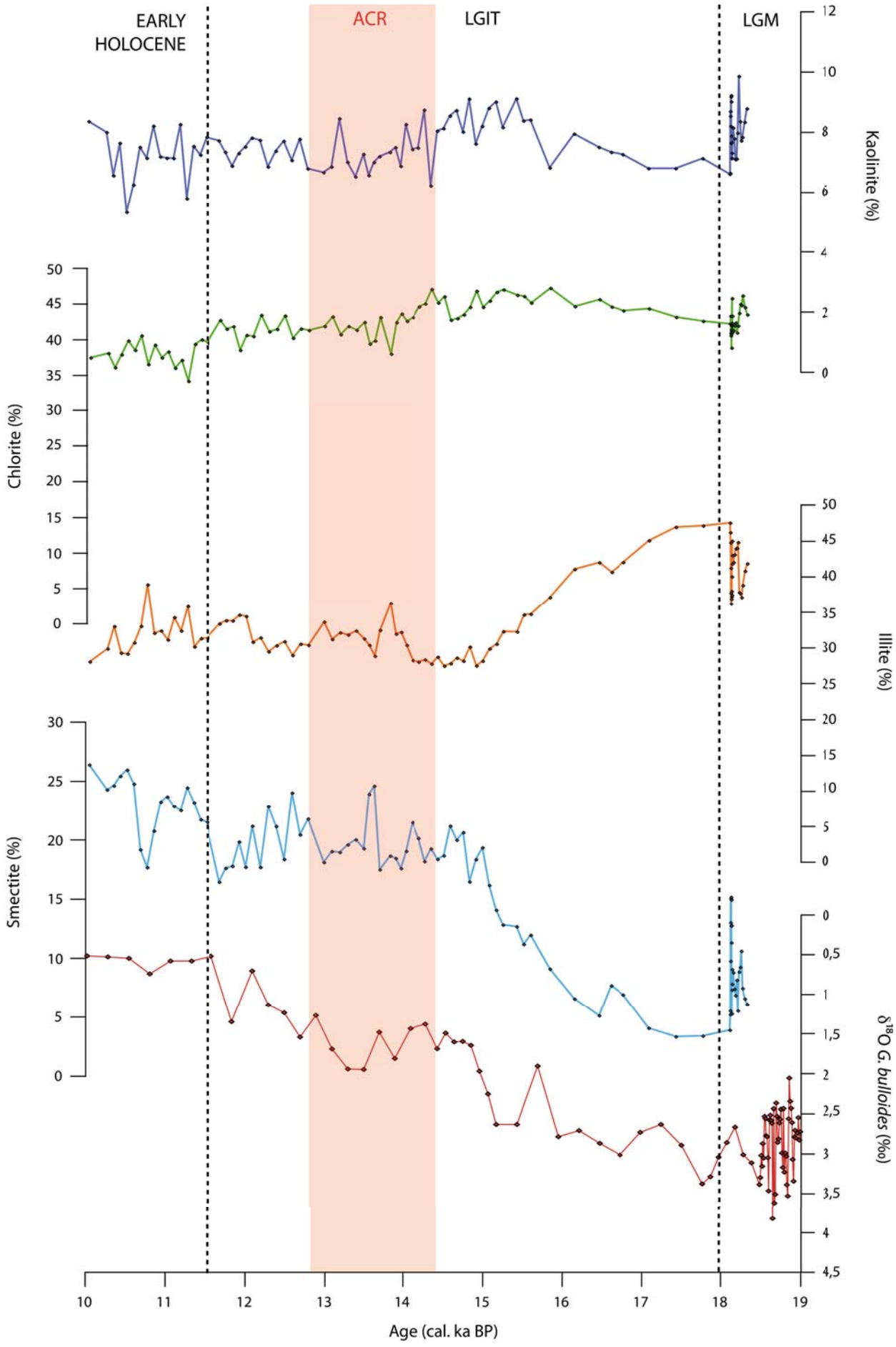

Figure 4: Distribution of the four main clay types of the core MD07-3119 as a function of time during the last glacial to deglacial period (22 to 10 ka BP) compared to the $\delta^{18}O$ record obtained from the plaktonic foraminifera *Globigerina bulloides*
LGM: Last glacial maximum; LGIT: Last glacial-interglacial transition; ACR: Antarctic Cold Reversal event

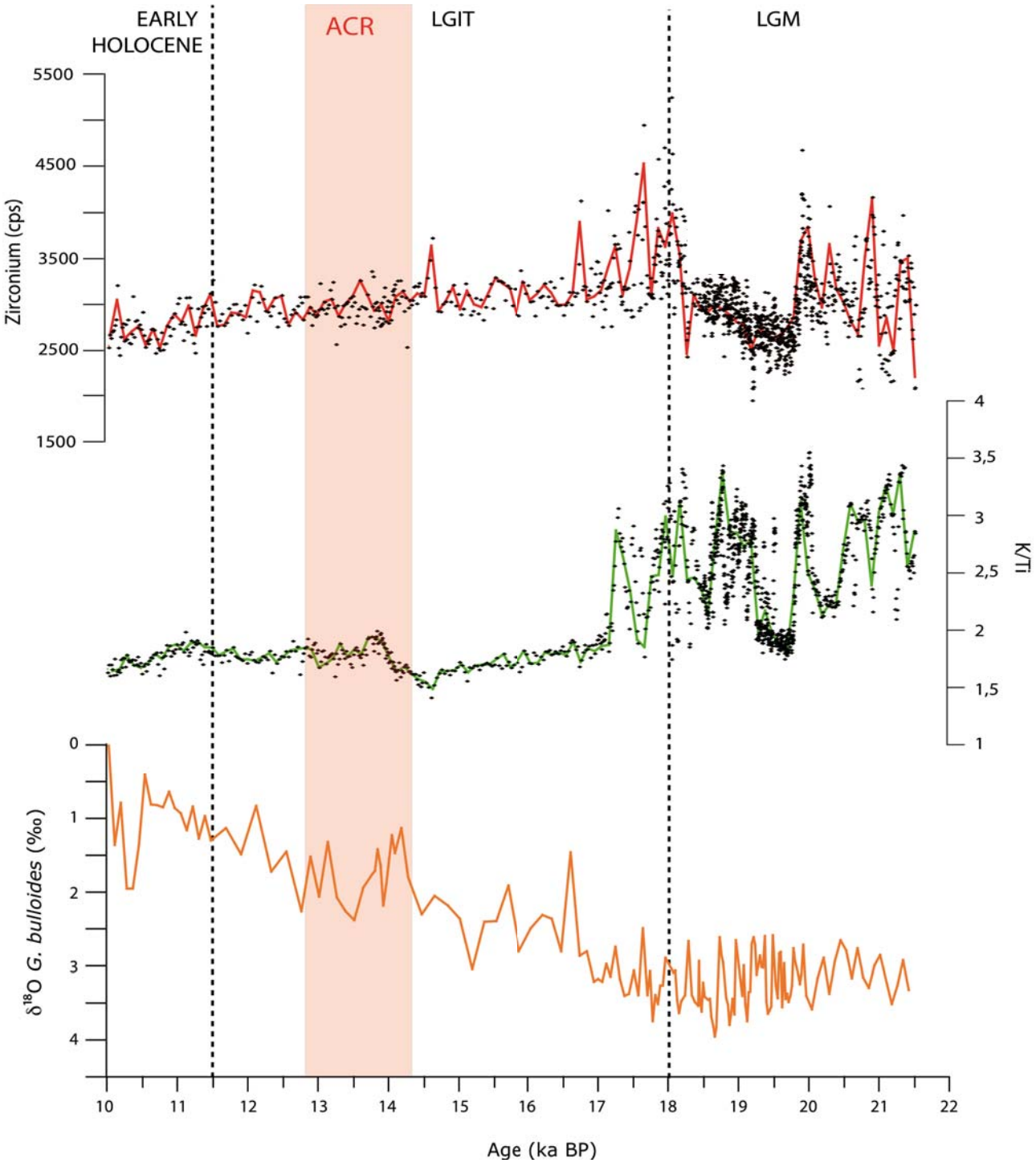

Figure 5: K/Ti ratio and Zr content (cps) obtained by XRF on bulk sediment in the core MD07-3088 compared to the $\delta^{18}O$ record obtained from the plaktonic foraminifera *Globigerina bulloides*
LGM: Last glacial maximum; LGIT: Last glacial-interglacial transition; ACR: Antarctic Cold Reversal event

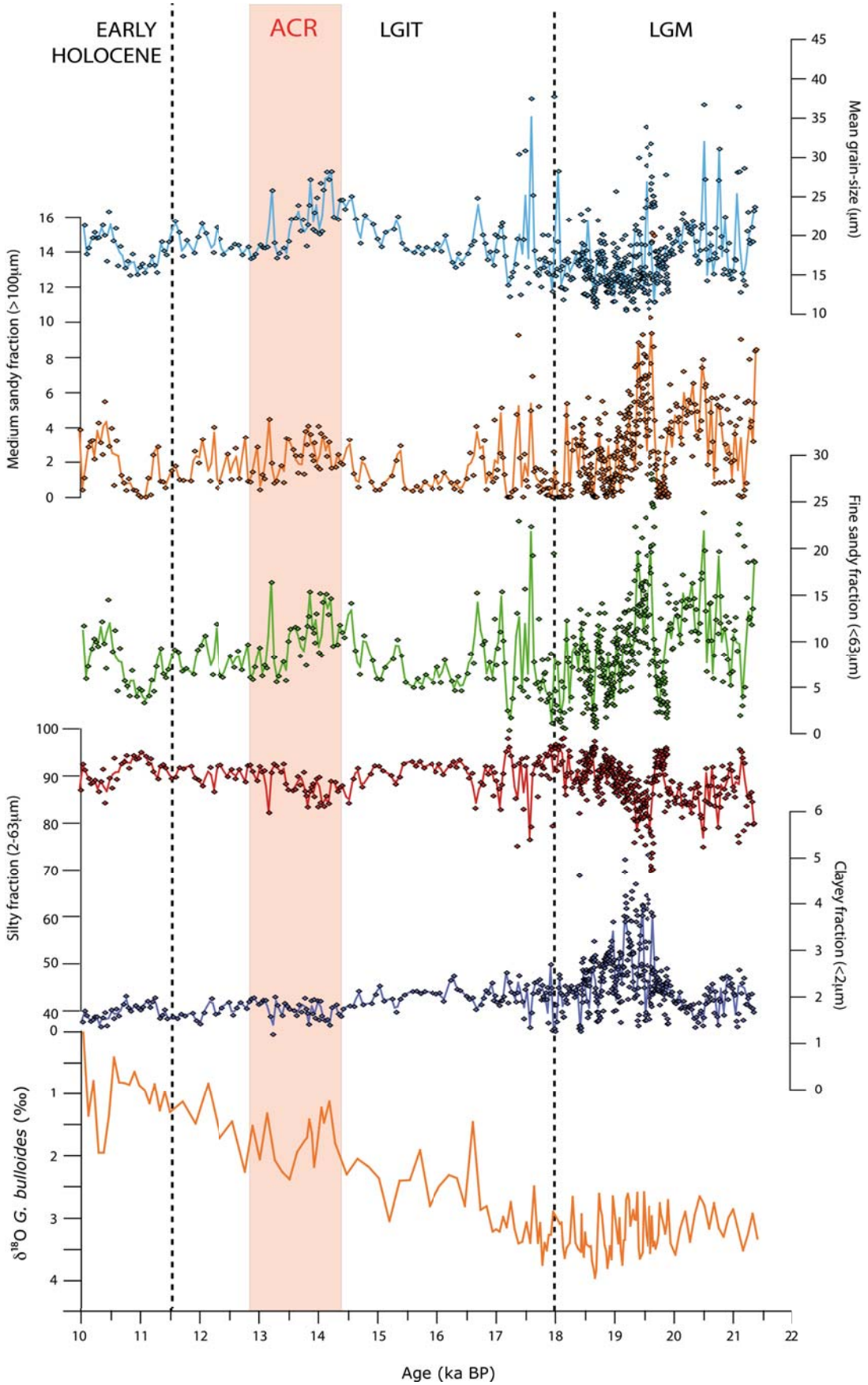

Figure 6: Grain size distribution of the clayey (< 2 µm), silty (2-63 µm), fine sandy (> 63 µm), medium sandy (> 100 µm) fractions and the mean grain-size (µm) of the core MD07-3088 since the LGM.

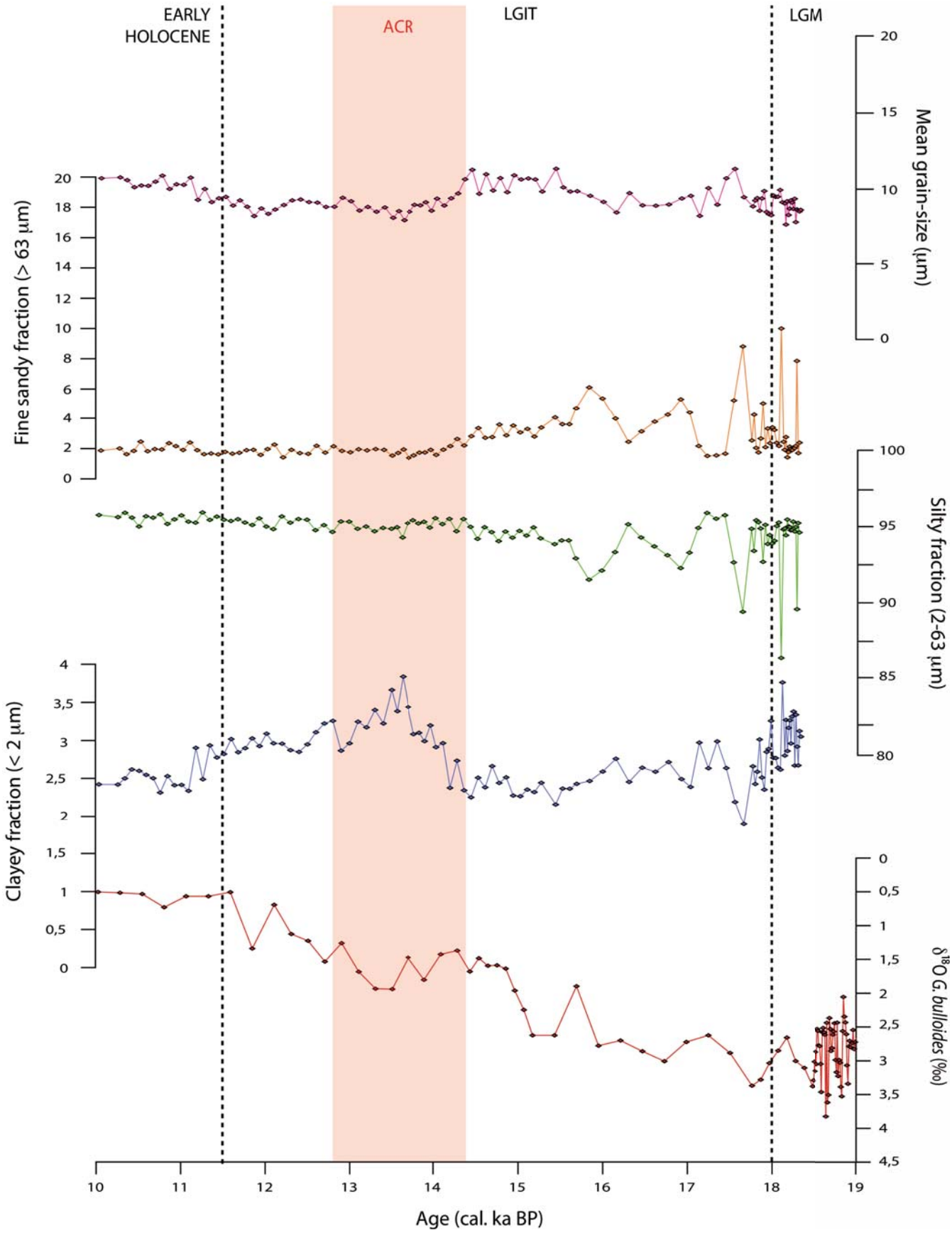

Figure 7: Grain size distribution of the clayey (< 2 µm), silty (2-63 µm), fine sandy (> 63 µm) fractions and the mean grain-size (µm) of the core MD07-3119 since the LGM.

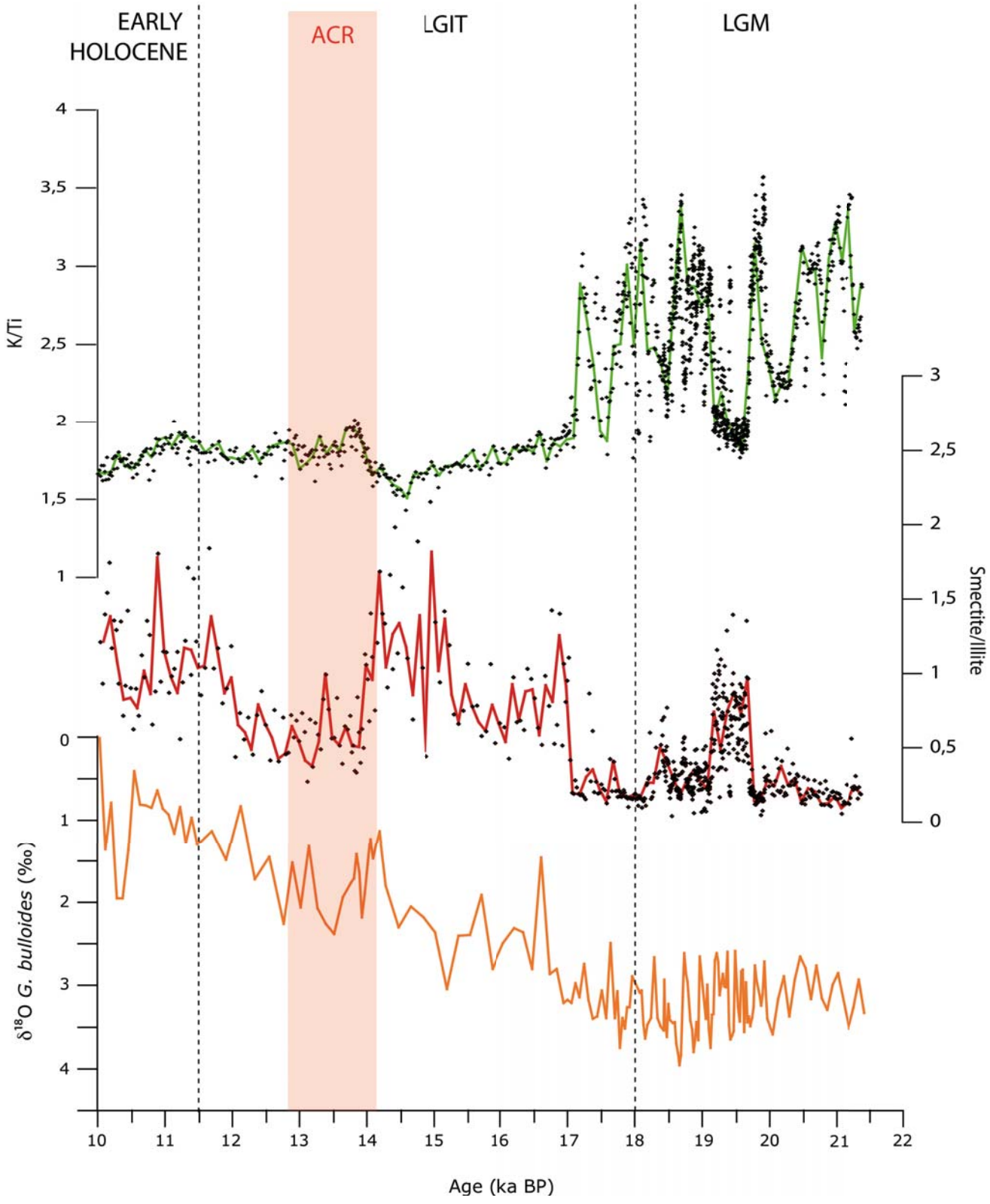

Figure 8: Comparison between smectite/illite and K/Ti ratios of the core MD07-3088 as proxies of the continental source since the LGM compared to oxygen isotope distribution.

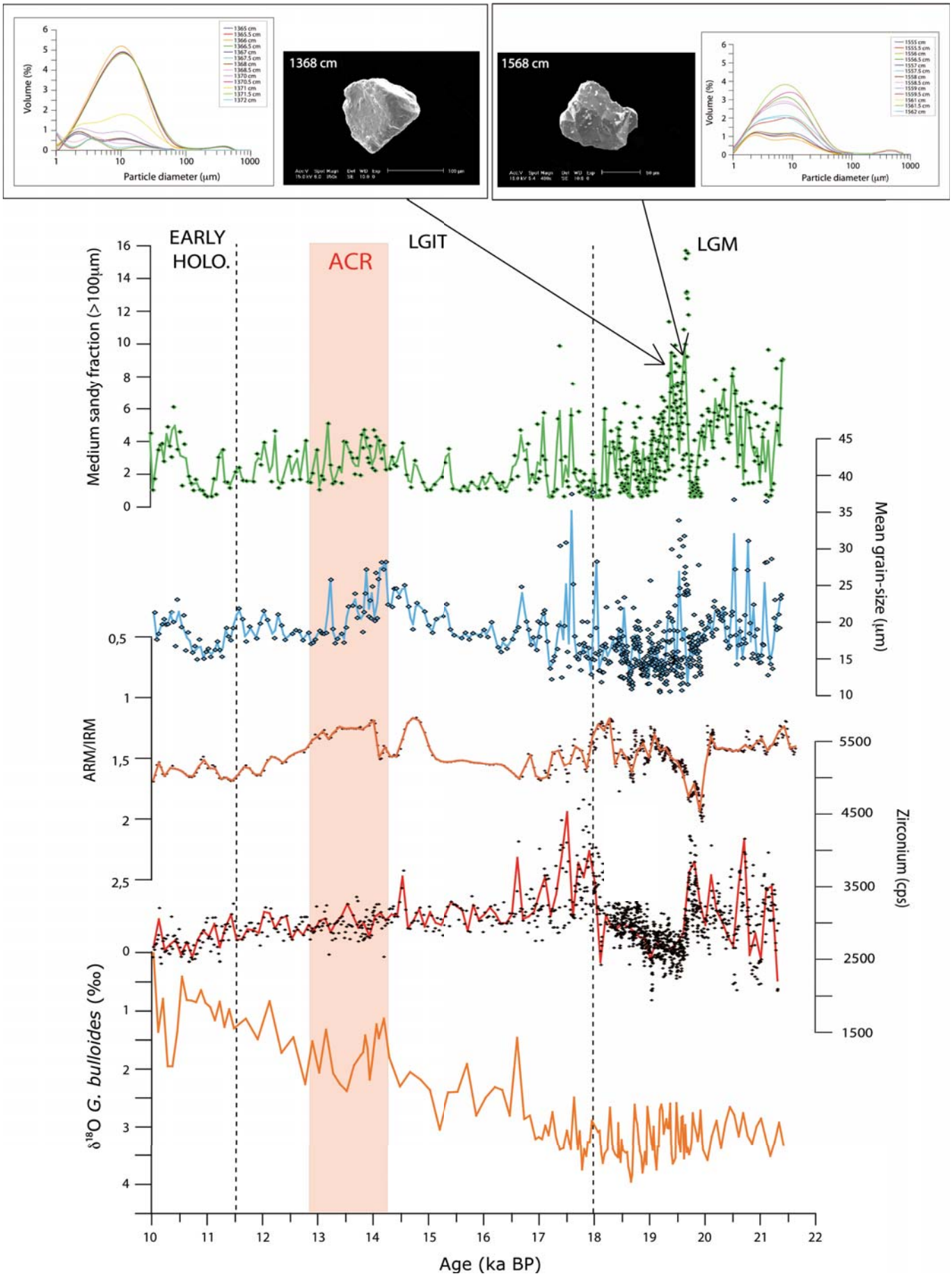

Figure 9: Comparison between Zr content (cps), magnetic parameters ARM/IRM ratio, mean grain-size and medium sandy fraction of the core MD07-3088 since the LGM. Inserts show particles shapes obtained by SEM imaging and respective grain-size diameter of detrital particles (quartz) of two coarser layers attributed to IRD events

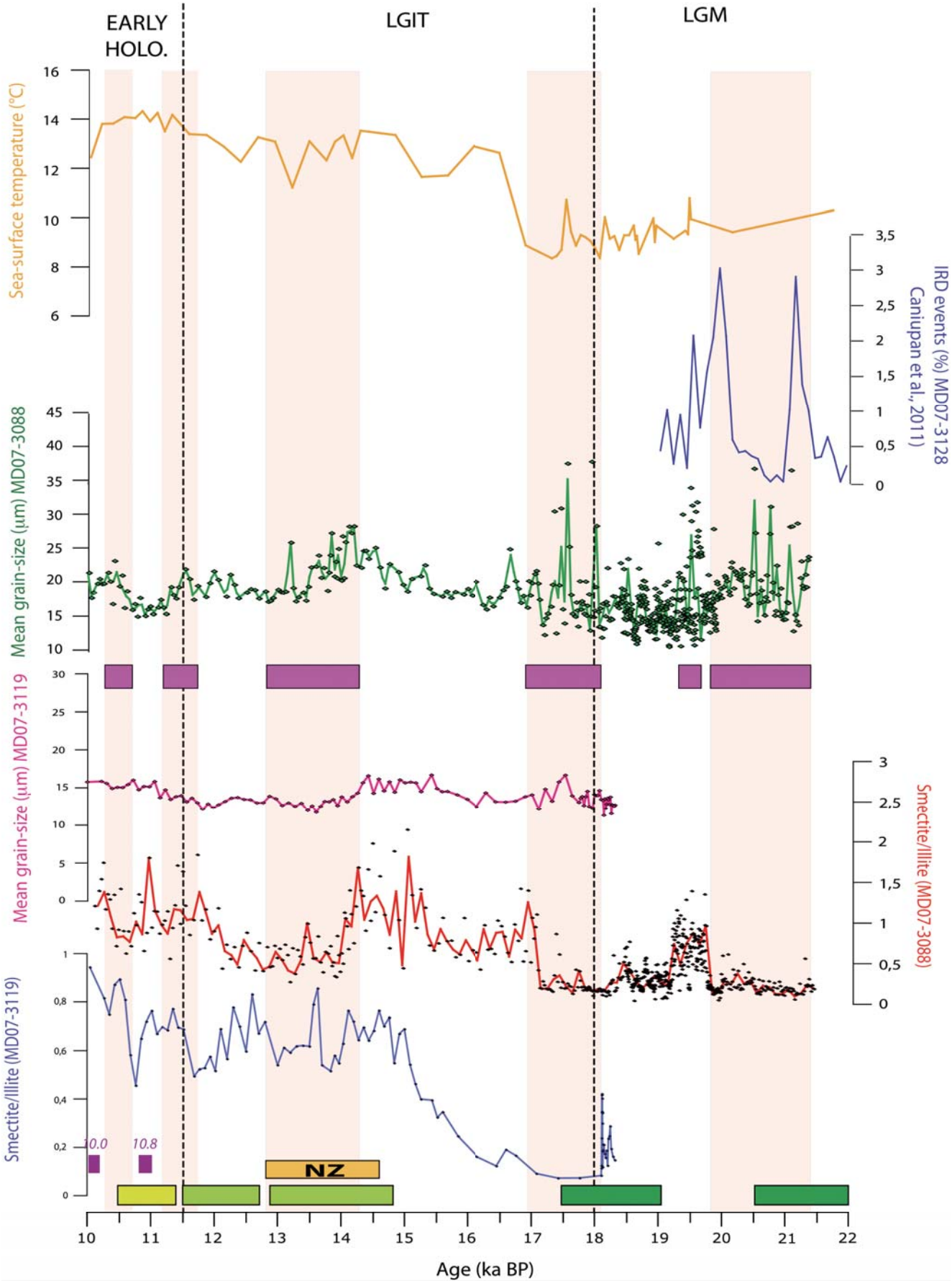

Figure 10: Smectite/illite ratios and mean grain size from deep-sea cores MD07-3119 and MD07-3088 compared to Nothofagus dombeyi pollens distributions from MD07-3088, sea-surface temperatures from MD07-3088 and Termination I glacier advances (Dark green: McCulloch et al., 2005; medium green: Aniya, 1995; Glasser et al., 2004; 2006; Moreno, 2009; Kaplan et al., 2011; Sagredo et al., 2011; light green: Glasser et al., 2006; purple: Carel et al., in prep. and orange: Putnam et al., 2010; 2012); Pink boxes represent glacier advances identified in the cores MD07-3088 and/or MD07-3119

Depth (cm)	Species	^{14}C age	± 1σ	Calibrated age (cal. BP)
610	*G. bulloides*	10050	35	10450
660	*G. bulloides*	10880	35	11300
700	*G. bulloides*	11765	35	12760
750	*G. bulloides*	12885	40	13840
780	*G. bulloides*	13185	45	14085
800	*G. bulloides*	13755	35	14465
810	*G. bulloides*	13840	45	14835
830	*G. bulloides*	14290	50	15530
850	*G. bulloides*	14560	50	16205
870	*G. bulloides*	14970	80	16735
880	*G. bulloides*	15145	50	16935
900	*G. bulloides*	15365	50	17175
940	*G. bulloides*	15540	70	17700
990	*G. bulloides*	15590	50	18065
1020	*G. bulloides*	15755	50	18235
1040	*G. bulloides*	16295	45	18420
1170	*G. bulloides*	16320	45	18730
1710	*G. bulloides*	17610	50	19960
1890	*G. bulloides*	18800	60	21415

Table 1: Conventional radiocarbon ages obtained by AMS dating on monospecific planktonic foraminifera *G. bulloides* of the core MD07-3088. Calendar ages were converted using CALIB 6.0. software (Reimer et al., 2009).

Depth (cm) MD07-3119	Depth (cm) MD07-3088	Species	Calibrated age (cal. BP)
10	440	*G. bulloides*	7358
60	480	*G. bulloides*	8076
140	495	*G. bulloides*	8345
180	525	*G. bulloides*	8944
210	540	*G. bulloides*	9250
320	685	*G. bulloides*	12115
390	730	*G. bulloides*	13510
435	795	*G. bulloides*	14390
510	820	*G. bulloides*	15183
610	950	*G. bulloides*	17773
680	1005	*G. bulloides*	18491
840	1140	*G. bulloides*	18657

Table 2: Correlation of the depth between the cores MD07-3088 and MD07-3119 and analogues conventional radiocarbon ages obtained by AMS dating on monospecific planktonic foraminifera *G. bulloides* in the core MD07-3088. Calendar ages were converted using CALIB 6.0. software (Reimer et al., 2009).